

**Simulation of X-ray projections on GPU: benchmarking gVirtualXray with clinically realistic phantoms**

Pointon, Jamie; Wen, Tianci; Tugwell-Allsup, Jenna; Sujar, Aaron; Létang, Jean Michel; Vidal, Franck

Computer Methods and Programs in Biomedicine

DOI:

[10.1016/j.cmpb.2023.107500](https://doi.org/10.1016/j.cmpb.2023.107500)

Published: 01/06/2023

Peer reviewed version

[Cyswllt i'r cyhoeddiad / Link to publication](#)

Dyfyniad o'r fersiwn a gyhoeddwyd / Citation for published version (APA):

Pointon, J., Wen, T., Tugwell-Allsup, J., Sujar, A., Létang, J. M., & Vidal, F. (2023). Simulation of X-ray projections on GPU: benchmarking gVirtualXray with clinically realistic phantoms.

Computer Methods and Programs in Biomedicine, 234, Article 107500.

<https://doi.org/10.1016/j.cmpb.2023.107500>

Hawliau Cyffredinol / General rights

Copyright and moral rights for the publications made accessible in the public portal are retained by the authors and/or other copyright owners and it is a condition of accessing publications that users recognise and abide by the legal requirements associated with these rights.

- Users may download and print one copy of any publication from the public portal for the purpose of private study or research.
- You may not further distribute the material or use it for any profit-making activity or commercial gain
- You may freely distribute the URL identifying the publication in the public portal ?

Take down policy

If you believe that this document breaches copyright please contact us providing details, and we will remove access to the work immediately and investigate your claim.

Simulation of X-ray projections on GPU: benchmarking gVirtualXray with clinically realistic phantoms

Jamie Lea Pointon^a, Tianci Wen^a, Jenna Tugwell-Allsup^b, Aaron Sújara^{c,a},
Jean Michel Létang^d, Franck Patrick Vidal^{a,1}

^a*School of Computer Science & Electronic Engineering, Bangor University, UK*

^b*Radiology Department, Betsi Cadwaladr University Health Board (BCUHB), North Wales, Ysbyty Gwynedd, UK*

^c*Department of Computer Science, Universidad Rey Juan Carlos, Mostoles, Spain*

^d*Univ Lyon, INSA-Lyon, Université Claude Bernard Lyon 1, UJM-Saint Etienne, CNRS, Inserm, CREATIS UMR 5220, U1294, F-69373, LYON, France*

Abstract

Background and Objectives: This study provides a quantitative comparison of images created using gVirtualXray (gVXR) to both Monte Carlo (MC) and real images of clinically realistic phantoms. gVirtualXray is an open-source framework that relies on the Beer-Lambert law to simulate X-ray images in realtime on a graphics processor unit (GPU) using triangular meshes.

Methods: Images are generated with gVirtualXray and compared with a corresponding ground truth image of an anthropomorphic phantom: (i) an X-ray projection generated using a Monte Carlo simulation code, (ii) real digitally reconstructed radiographs (DRRs), (iii) computed tomography (CT) slices, and (iv) a real radiograph acquired with a clinical X-ray imaging system. When real images are involved, the simulations are used in an image registration framework so that the two images are aligned.

Results: The mean absolute percentage error (MAPE) between the images simulated with gVirtualXray and MC is 3.12%, the zero-mean normalised cross-correlation (ZNCC) is 99.96% and the structural similarity index (SSIM) is 0.99. The run-time is 10 days for MC and 23 ms with gVirtualXray. Images simulated using surface models segmented from a CT scan of the Lungman chest phantom

*Corresponding author

Email address: `f.vidal@bangor.ac.uk` (Franck Patrick Vidal)

were similar to i) DRRs computed from the CT volume and ii) an actual digital radiograph. CT slices reconstructed from images simulated with gVirtualXray were comparable to the corresponding slices of the original CT volume.

Conclusions: When scattering can be ignored, accurate images that would take days using MC can be generated in milliseconds with gVirtualXray. This speed of execution enables the use of repetitive simulations with varying parameters, e.g. to generate training data for a deep-learning algorithm, and to minimise the objective function of an optimisation problem in image registration. The use of surface models enables the combination of X-ray simulation with real-time soft-tissue deformation and character animation, which can be deployed in virtual reality applications.

Keywords: X-rays, Computed tomography, Simulation, Monte Carlo, GPU programming, Image registration, DRR

1. Introduction

Monte Carlo (MC) simulation is known as the state-of-the-art technique to simulate X-ray images in terms of accuracy. However, prohibitive computing time may be required to simulate an X-ray projection at high spatial resolution with an acceptable level of noise, which limits the use of MC simulations in applications where real-time performance is a requirement [1]. Badal and Badano [2] adapted PENELOPE’s MC code to graphics processor unit (GPU) computing in 2009. In the example they provided, they simulated an image with 150×300 pixels using 10^{10} primary X-rays. They reported runtimes in minutes incompatible with real-time performance: i) 5106 on a central processor unit (CPU) for the original PENELOPE’s code, ii) 624 for their simplified CPU implementation, iii) 83 for a GPU with no fast math, iv) 60 for a GPU with fast math and v) 24 for a GPU with single-precision floating-point numbers. In 2022, Mettivier et al. [3] developed a GPU-based Monte Carlo X-ray simulator. They generated computed tomography (CT) scan acquisition data on a high-performance GPU (NVIDIA GeForce RTX™ 3090). They reported

that almost 3 hours of computations are needed to create 360 projections of $1,900 \times 1,900$ pixels from a $385 \times 385 \times 214$ voxelised phantom, i.e. almost half a minute per projection. Whilst GPU-based MC simulations are extremely fast compared to their CPU counterparts (about $1,000\times$ faster), there are still far from real-time performance. About 13 seconds are necessary to compute the voxel dose distribution in a $122 \times 62 \times 372$ volume, which is relatively small compared to a typical CT volume [4]. Voxelised models are often a requirement, although surface meshes (STL files) are now supported in GATE¹ [5]. It is an open-source software dedicated to numerical simulations in medical imaging and radiotherapy based on Geant4², the general-purpose MC code by the European Organization for Nuclear Research (CERN). In this case, each surface mesh is converted into a tessellated volume [6]. Note that it is possible to disable physics processes, such as scattering, in MC methods to speed up X-ray generation. In this case, the resulting images are similar to those produced by deterministic methods but with noise.

Deterministic simulations based on the Beer-Lambert law generate noise-free images. Depending on the application, they can provide a good compromise between speed and accuracy [7] and can be implemented on GPUs for a further increase of speed [8, 9]. Unlike Monte Carlo methods, deterministic simulations tend to ignore scattering and noise, although the latter can easily be added as a post-process. In this paper, gVirtualXray (gVXR)³ is used. It is an open-source library written in C++ and the OpenGL Shading Language (GLSL). gVirtualXray is portable and works on a wide range of computers and operating systems (from Windows laptops to GNU/Linux Supercomputers). Wrappers to other popular languages, including Python⁴, R, Ruby, C#, Java and GNU Octave, are also available. The Analytical RT Inspection Sim-

¹<http://www.opengatecollaboration.org/> (accessed: 27 February 2023)

²<https://geant4.web.cern.ch/> (accessed: 27 February 2023)

³<https://sourceforge.net/projects/gvirtualxray/> (accessed: 27 February 2023)

⁴<https://pypi.org/project/gVXR/> (accessed: 27 February 2023)

ulation Tool (aRTist)⁵ developed by Bundesanstalt für Materialforschung und prüfung (BAM, Germany) also makes use of a deterministic method to simulate X-ray projections from computer-aided design (CAD) models [10]. It provides a graphical user interface (GUI) and is dedicated to nondestructive testing (NDT) for industrial applications. CIVA by Extende⁶ also uses a deterministic method to simulate X-ray or γ -ray projections. Both aRTist and CIVA are closed-source commercial software with a license fee.

The combination of deterministic modelling with GPU computing allows high-resolution X-ray projections to be simulated without scattering and without noise in a few microseconds, which opens up new perspectives and opportunities. It is possible to use gVirtualXray in real-time applications such as medical training simulators (see Figures 1a and 1b) [11, 12, 13]. GPUs also make it possible to embed gVirtualXray within an optimisation algorithm to register 3D hand models on 2D radiographs [14] or produce accurate digital twins in material science [15]. gVirtualXray can also be used to produce a high number of realistic simulated images to train machine learning algorithms [16, 17], which would not have been possible a few years ago. Albiol et al. [18] proposed a new type of densitometric radiographic images (a technique that combines two radiographs that were produced with two different tube voltages). They replaced one of the radiographs with a simulated one, thanks to the use of a contour sensor (e.g. Microsoft Kinect) and gVirtualXray (see Figure 1c). It is also possible to integrate further simulation models to take into account the patient’s physiology such as the respiration during the CT scan acquisition. In this case, reconstructed slices will exhibit motion artefacts [19]. Andreozzi et al. [20] used gVirtualXray to generate noise free X-ray radiographs. Noise is added as a post-process to study real-time edge-aware denoising in fluoroscopic devices. Corbi integrated gVirtualXray with other relevant software packages,

⁵<https://artist.bam.de/> (accessed: 27 February 2023)

⁶<https://www.extende.com/radiographic-testing-with-civa> (accessed: 27 February 2023)

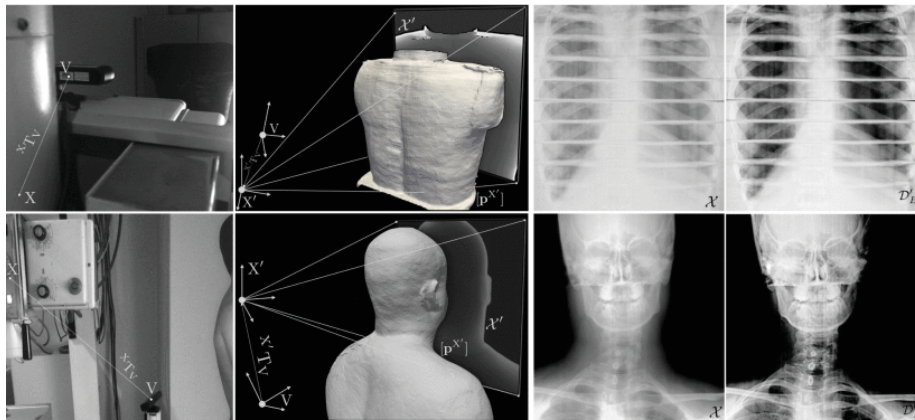
such as Geant4, into a Docker container that is used online to teach particle physics and X-ray imaging to undergraduate students in engineering [21].



(a) Orthopaedic surgical simulator providing user-controlled image intensifier functionality. Reproduced with permission from Racy et al. [12].



(b) Radiography teaching tool with real-time character animation and soft-tissue deformations to interactively change the patient's pose in simulated X-ray radiographs.



(c) Examples of virtual densitometric image (D'_B , 4th column). 1st column: experimental setup. 2nd column: iso-surfaces from the depth sensor. Virtual (high-energy) water-equivalent radiographs (\mathcal{X}') from water-filled volumes [$\mathbf{p}\mathcal{X}'$]. 3rd column: original radiographs (\mathcal{X}). Top row: chest section of a RANDO anthropomorphic phantom (105 kVp and 6 mAs). The horizontal lines correspond to the inter-slice separations. Bottom row: real patient (55 kVp and 9 mAs). Reproduced with permission from Albiol et al. [18].

Figure 1: Examples of medical applications using gVirtualXray as a core component.

To date, gVirtualXray has been validated using extremely simplistic MC simulations of a cube of water in which a bone cylinder was inserted [9]. There is no direct comparison between images simulated with gVirtualXray and (i) real images or (ii) images simulated by a Monte Carlo method with clinically

realistic acquisition parameters and anthropomorphic phantoms. The aim of this paper is to address these limitations. The assumption is that X-ray images simulated in milliseconds with a deterministic algorithm on GPU are realistic for clinical applications where speed is a requirement, whether this is virtual reality (VR) simulators where X-ray images must be simulated in realtime from dynamic patient models, or high-throughput data processing where a massive amount of data must be generated very quickly. Another motivation, from an educational point of view, is that exposure parameters have an influence not only on image quality but also on the radiation dose the patient receives. Using anthropomorphic phantoms with realistic clinical parameters to develop a virtual software is important to recognise the effect those parameters have on image quality in terms of contrast and noise from the absorption and scattering of the X-ray photons.

To benchmark X-ray projections simulated on GPU with gVirtualXray against ground truth images of clinically realistic phantoms:

- A suitable digital anthropomorphic phantom must be chosen. It will be used to compare i) an X-ray projection using gVirtualXray with ii) an image simulated using a state-of-the-art MC simulation tool. MC simulation is considered the gold standard method in particle physics. MC methods are based on step-by-step transportation and tracking of particles. The open-source software GATE v9.0 [5] based on the Geant4 v10.7 toolkit [22] has been used in this study. Option 4 of the electromagnetic standard library was selected, following the recommendation from the Geant4 medical simulation benchmarking group [23]. Simulation parameters for both simulations must be equivalent.
- A suitable anthropomorphic phantom used in clinical routine must be selected. It corresponds to some kind of mannequin that can be scanned. The virtual anatomy is extracted by segmentation and isosurfacing of the CT scan of the phantom. It is used to produce another two simulated radiographs. They will be compared with digitally reconstructed radio-

graphs (DRRs) computed from the original CT scan of the anthropomorphic phantom. DRRs are radiographic images produced directly from 3D CT data. They have been used in several medical imaging applications for decades, such as the verification of computer-designed radiotherapy treatments [24], 2D/3D image registration [25] and more recently the creation of training data for training tumour-tracking algorithms [26]. They are often computed using a ray-casting algorithm and tend to ignore scattering although it can be taken into account [27]. The main difference between the simulations performed using gVirtualXray and DRRs is in the data representation of the scanned patient: surface meshes vs. voxels. Simulation parameters for the radiographs and corresponding DRRs must be equivalent.

- A CT data acquisition will be simulated. The anthropomorphic phantom data will be used as a CT scan of the phantom is available. The simulation will generate a set of 2D X-ray radiographs taken at successive angles around the phantom. When a sufficient number of projections is available, a traditional filtered-back projection (FBP) or Feldkamp, Davis and Kress (FDK) algorithm can be used to “convert” this set of 2D X-ray radiographs into a 3D CT volume. 2D CT slices extracted from the volume reconstructed from the simulated projections will be quantitatively compared to the corresponding slices of the original CT scan.
- A simulated radiograph will be registered using an optimisation algorithm so that it matches the image acquired with a clinically utilised equipment. The radiograph is taken from the anthropomorphic phantom utilised in clinical routine. Parameters of the real image acquisition (such as source-to-patient and source-to-detector distances) may be unknown or inaccurate values estimated by optimisation. This approach is a complex global optimisation problem where the shape of the search space and the derivative of the objective function are unknown. One of the difficulties is that radiographs used in clinical routine are always post-processed: i) they are

recorded in negative to mimic what used to happen when films were used, and ii) an undocumented image sharpening filter is applied to highlight edges between anatomical structures.

2. Methods and materials

2.1. Overview of the simulation model

In clinical routine, an anti-scatter grid is commonly used in radiography. It is a device placed between the patient and the detector. Such devices use a grid pattern designed to stop scattered photons and let through the photons that travel along a straight line from the source to the detector. CT scanners in medicine make use of a helical scanning geometry where the patient couch is continuously translated during the data acquisition [28]. It allows the beam to be collimated to a fan-beam geometry rather than a large rectangular area. It significantly reduces the amount of scattered radiation compared to cone-beam computed tomography (CBCT), which requires a 2D area detector with many more rows of pixels. Scatter in CT does occur and causes inaccuracies in the measurement of attenuation values which can lead to artefacts such as cupping, streaks, increased image noise, uniformity issues. Many correction methods are applied during CT reconstruction to account for these such as special filters but mainly in the reconstruction algorithm post processing. If scattering is neglected and an ideal (i.e. dirac) point-spread function is assumed, X-ray projections $\mathbf{I}(x, y)$ can simply be modelled with the Beer-Lambert attenuation law:

$$\mathbf{I}(x, y) = \sum_i \mathbf{R}(E_i) \mathbf{D}(E_i) \exp \left(- \sum_j \mu_j(E_i) \mathbf{d}_j(x, y) \right) \quad (1)$$

$\mathbf{I}(x, y)$ is the integrated energy in eV received by pixel (x, y) . In the polychromatic case, the beam spectrum is discretised in several energy channels. E_i corresponds to the energy in eV of the i -th energy channel. $\mathbf{D}(E_i)$ is the number of photons emitted by the source at that energy E_i . The detector response $\mathbf{R}(E_i)$ mimics the use of a scintillator by replacing the incident energy E_i with

a smaller value, i.e. $\mathbf{R}(E_i) < E_i$ (see Figure 6b for an example). The detector response is assumed space-invariant in Equation 1. j indicates the j -th material being scanned when a multi-material “object” is considered. $\mu_j(E_i)$ is the linear attenuation coefficient in cm^{-1} of the j -th material at energy E_i . $\mathbf{d}_j(x, y)$ is the path length in cm of the ray from the X-ray source to pixel (x, y) crossing the j -th material.

It is straightforward to implement the Beer-Lambert attenuation law using ray-tracing. However, such a naive approach misses the opportunity to take advantage of what GPUs are for: Draw millions of polygons as fast as possible in video games without the need to explicitly compute ray-triangle intersections. Traditionally, an image is generated in 3D video games in two successive main steps : i) triangles are transformed (e.g. translation, scaling, rotation, projection), and ii) pixel colours are computed. Let us consider the simple simulation presented in Figure 2. It is used to illustrate how Eq. 1 is split into successive

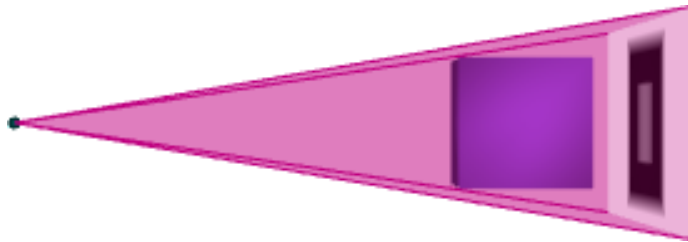


Figure 2: A simple simulation. The dot on the left-hand side depicts the X-ray source. The transparent pink shape shows the X-ray beam. The cube in magenta is the object being imaged. The detector can be seen on the right-hand side. One can see that a cylindric void is inside the cube.

steps in gVirtualXray. \mathbf{d}_j is computed per vertex and pixel values obtained by bi-linear interpolation. Figure 3a shows the corresponding image generated for the simulation presented in Figure 2. It is used to generate another temporary image that stores $\sum_j \mu_j \mathbf{d}_j$ (see Figure 3b). The simulated X-ray image can eventually be generated (see Figure 3c). Details about our implementation are already available for the monochromatic Beer-Lambert law [8], the polychromatic Beer-Lambert law and focal spots of the X-ray source [29], and adaptive

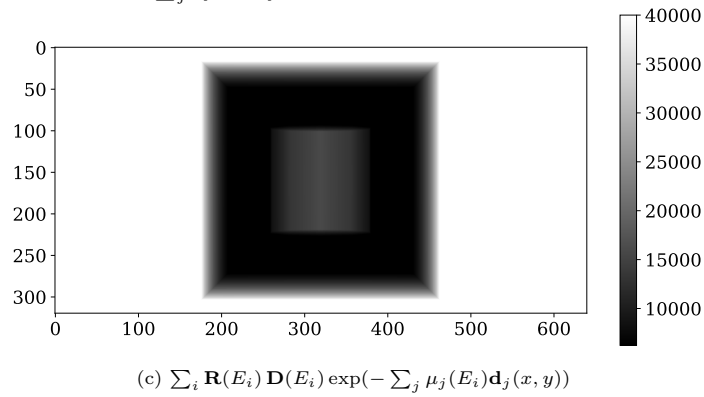
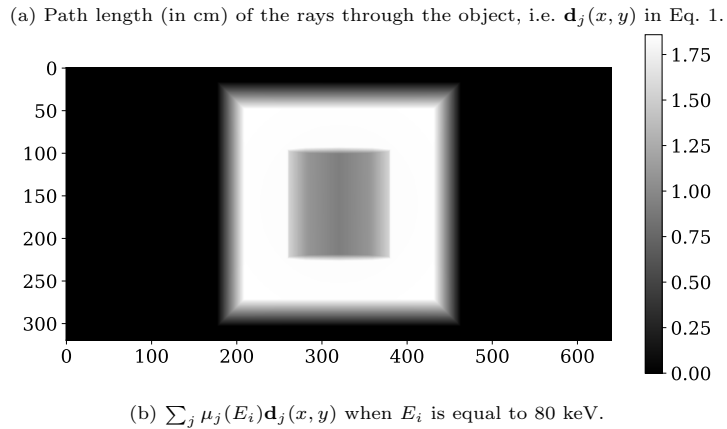
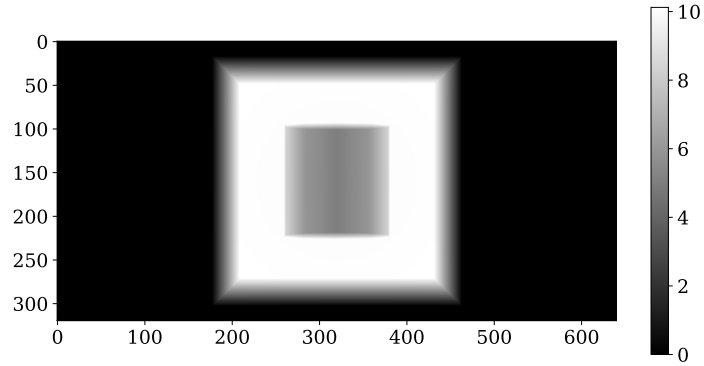


Figure 3: Successive images produced in the graphics pipeline for the simulation presented in Figure 2.

filtering to suppress errors that can arise due to GPU programming [9].

Known bottlenecks are (i) the number of polygons in the scanned geometry when computing \mathbf{d}_j , and (ii) the pixel resolution when computing $\mathbf{R}(E_i)\mathbf{D}(E_i)\exp(\dots)$. By convention in computer graphics, vectors normal to the surface of 3D objects are outward (see Figure 4). Freud et al. [30] took

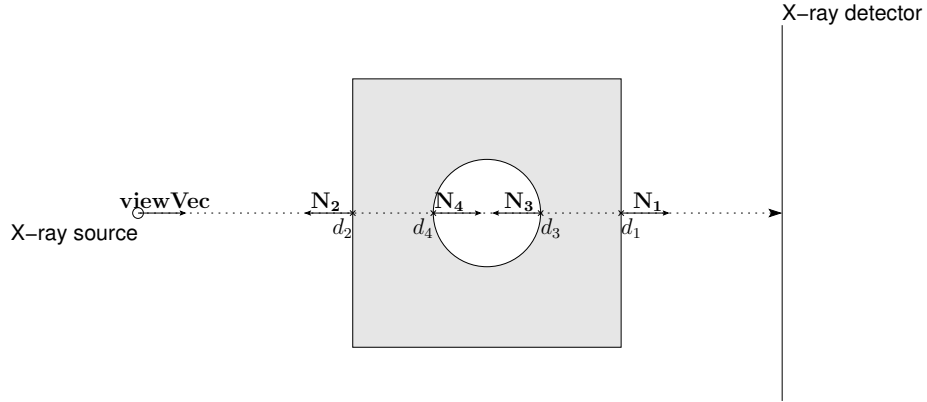


Figure 4: Principle of the computation of the L-buffer.

advantage of this principle to compute \mathbf{d}_j in Eq. 1. gVirtualXray relies on this technique too. Let us consider the example of Figure 4. The object is a cube in which an empty cylinder is included. There are 4 intersections between the ray and the object. Intersections may be detected in any order. The path length between the ray and the object is:

$$\mathbf{d} = (d_4 - d_2) + (d_1 - d_3) \quad (2)$$

where d_1, d_2, d_3 and d_4 correspond to the distance between the X-ray source and the corresponding intersections. The dot product between $-\mathbf{viewVec}$ and both \mathbf{N}_2 and \mathbf{N}_3 is positive. It is negative for both \mathbf{N}_4 and \mathbf{N}_1 . When the ray enters an object, this dot product is positive; it is negative when it exits an object. The L-buffer can be efficiently computed on GPU using ‘blending’, a function of graphics cards to display transparent objects without sorting triangles (or here intersections):

$$\mathbf{d} = \sum_k -\text{sgn}(-\mathbf{viewVec} \cdot \mathbf{N}_k) \times d_k \quad (3)$$

where k refers to the k^{th} intersection found in an arbitrary order, d_k is the distance from the X-ray source to the intersection point of the ray with the triangle, $\text{sgn}(-\mathbf{viewVec} \cdot \mathbf{N}_{\mathbf{k}})$ stands for the sign of the dot product between $-\mathbf{viewVec}$ and $\mathbf{N}_{\mathbf{k}}$. This dot product and d_k must be computed for each intersection point. During the rendering stage, hidden surface removal algorithms such as Z-buffer and back-face culling are disabled so that every triangle of the polygon mesh is taken into account.

To solve Eq. 1, linear attenuation coefficients must be known. These are computed from the mass attenuation coefficients $\mu(E)/\rho$ and the material density ρ in $\text{g}\cdot\text{cm}^{-3}$. Mass attenuation coefficients are expressed in $\text{cm}^2\cdot\text{g}^{-1}$. They are energy dependent, but do not depend on the state of the material. The mass attenuation coefficient $\mu(E)/\rho$ for a given material m consisting of several elements l with given elemental weights ω_l is computed from the Bragg additivity rule over the l elements in its composition:

$$\left(\frac{\mu}{\rho}\right)_m = \sum_{l \in \text{elements}(m)} \omega_l \left(\frac{\mu}{\rho}\right)_m \quad (4)$$

For each test, we generate two or more images using two different methods. A list of tests is provided in Table 1. A ground truth image (\mathbf{Y}) will be created i) experimentally, ii) by Monte Carlo simulation, or iii) as a DRR of an actual CT scan. A test image ($\hat{\mathbf{Y}}$) will be simulated using gVirtualXray with parameters similar to the corresponding ground truth image. To make our research reproducible, we provide (i) our Monte Carlo simulation scripts, (ii) our gVirtualXray Python code in Jupyter notebooks, and (iii) our output data on Zenodo and GitHub at <https://github.com/effepivi/gvxxr-validation/>. As the Monte Carlo software (here Geant4 & GATE), the DRR software (Plastimatch) and gVirtualXray are all open-source, our research is therefore fully reproducible.

2.2. Anthropomorphic phantoms

We use two datasets from anthropomorphic phantoms: One is digital, one extracted from a CT volume.

Note to the reviewers: A DOI will be generated in due time if the paper is accepted

Table 1: Overview of the validation tests.

Notebook	Spectrum	Test object	Scintillator	Ground truth (Y)	Test
1	kVp: 85, anode: W, filtration: 0.1 mm of Cu & 1 mm of Al	5-year old boy	600 μm of CsI	GATE simulation, 10^9 photon	Simulation vs simulation
2	mono energy (72 keV)	Lungman	None	DRRs of original CT	Simulation vs. DRR
3	kVp: 100, anode: W, filtration: 2.5 mm of Al, 0.5 mm of Cu	Lungman	600 μm of CsI	Original CT	Simulation+reconstruction vs. CT
4	kVp: 90, anode: W, filtration: none	Lungman	600 μm of CsI	Digital radiography, exposure: 1 mAs, 5 ms	Registration of simulated image onto real image

2.2.1. *pEdiatRic dosimetRy personalized platfORm*

The phantom from the pEdiatRic dosimetRy personalized platfORm (ER-ROR) [31] is used in Notebook 1. It corresponds to the anatomy of a 5-year-old boy. It is provided as a labelled $512 \times 511 \times 190$ volume, which includes 24 different structures, such as air, muscle, bone, stomach-interior, cartilage, etc. Surface meshes (see Figure 5a) are generated from the labelled data using the Visualization Toolkit (VTK) [32]. The definitions of tissue substitutes are provided in the ICRU Report 44 by the International Commission on Radiation Units and Measurements [33].

2.2.2. *Lungman anthropomorphic chest phantom*

Notebooks 2, 3 and 4 make use of the Lungman anthropomorphic chest phantom (Kyoto Kagaku, Tokyo, Japan) [34]. Anthropomorphic phantoms allow for multiple exposures under consistent conditions to occur for all image acquisitions allowing radiation dose and image quality to be compared: We can therefore compare a digital radiograph taken using a clinically utilised device and an image simulated under the same conditions. The Lungman phantom represents a 70 kg male (see Figure 5b). The equivalence in terms of polymethyl methacrylate (PMMA) was established for the lung and mediastinum regions of the phantom. Tumours of various densities are embedded. The phantom is made of materials with X-ray absorption properties close to those of human tissue. In this way, results remain clinically relevant and accurate as X-ray energy is altered.

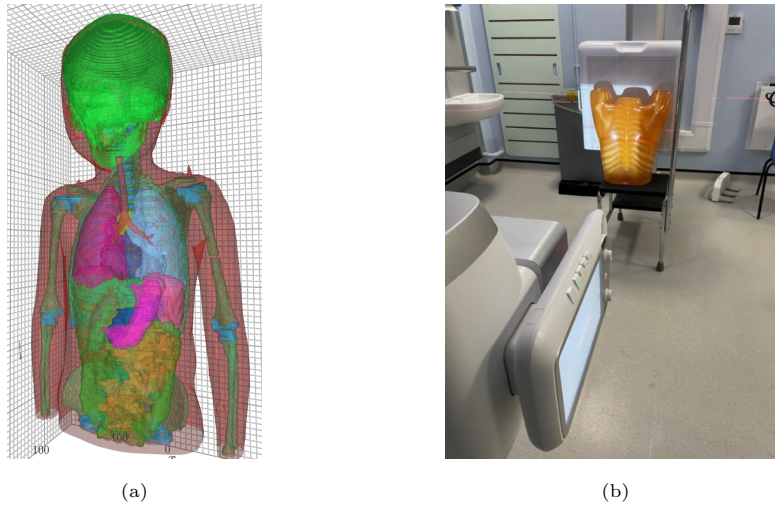


Figure 5: Anthropomorphic phantoms. (a) Paediatric phantom from the ERROR project. (b) Photography of the Lungman anthropomorphic phantom and the clinically utilised X-ray equipment used in our study.

First, a digital phantom must be created. A CT scan of the Lungman phantom was acquired at one of our local hospitals (Ysbyty Gwynedd) using a 128-slice Somatom Definition Edge scanner, Siemens Healthcare, Erlangen, Germany. The CT volume was then segmented into individual structures. The problem of over-segmentation is mitigated by creating eroded masks for each label volume, i.e. using mathematical morphology. This ensures that the masks do not span over different structures which could result in a coefficient that does not best represent its material composition. For each mask, a surface mesh was extracted. The aggregate of all the surface meshes forms a computational model of the scanned sample or patient. Open-source toolkits, the Insight Toolkit (ITK) [35] and VTK [32], have been used for all image processing operations.

Simulating X-ray projections using gVirtualXray requires X-ray attenuation properties for each structure to be chosen. Voxels of medical CT volumes are in Hounsfield Unit (HU). The mean value computed from masking the CT with each surface is assigned to their respective structure. Hounsfield values are then converted into material composition and densities using Schneider et al. [36]'s

method. Whilst it has not been calibrated for the CT scanner used in our experiment, it provides a plausible approximation.

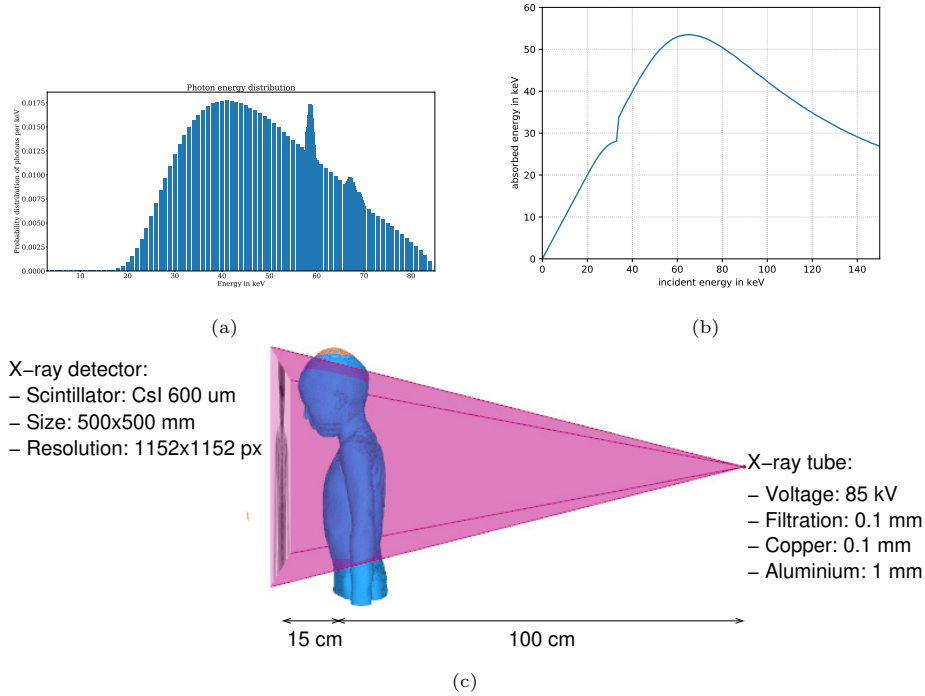


Figure 6: (a) Photon energy distribution of the X-ray source. Tube voltage: 85 kV. Filtration: 0.1 mm of copper and 1 mm of aluminium. (b) Energy response of the detector. It mimics a 600-micron thick CsI scintillator. (c) Simulation parameters.

2.3. Notebook 1: Comparison of radiographs of an anatomically realistic 5-year-old boy simulated with GATE and gVirtualXray

Figure 6c summarises the simulation parameters. The source-to-object distance (SOD) is 100 cm, and the source-to-detector distance (SDD) is 112.5 cm. The beam spectrum is polychromatic (see Figure 6a). The tube voltage is 85 kV. The anode is made of tungsten. The filtration is 0.1 mm of copper and 1 mm of aluminium. The energy response of the detector is considered. It mimics a 600-micron thick CsI scintillator (Figure 6b). For the Monte-Carlo simula-

tions, the number of photons impinging the detector was set to 10^9 and directly transmitted photons have been saved separately from scattered ones.

2.4. Notebook 2: DRR from CT volume vs. X-ray simulation using surface meshes extracted from segmented CT volume

It is possible to extract surface meshes from a segmented CT scan, simulate an X-ray projection with gVirtualXray and compare it with the corresponding DRR computed from the original CT scan. The main steps are summarised in Figure 7.

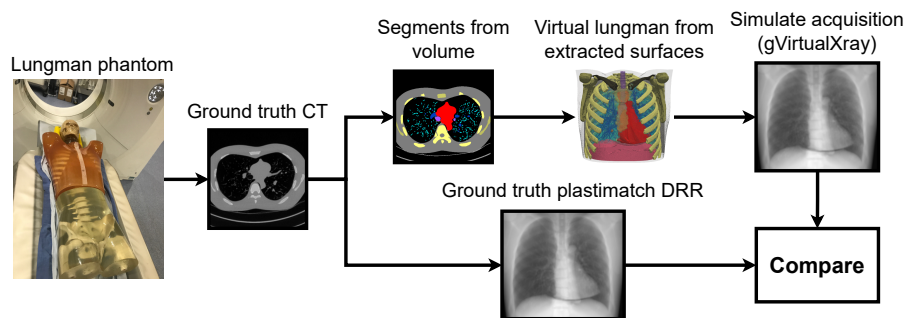


Figure 7: Flow chart demonstrating the validation of projections of the Lungman simulated with gVirtualXray process.

Plastimatch was used to generate DRRs [37]. It is an open-source software for image computation, with a focus on high-performance volumetric registration of medical images. It is developed at the Department of Radiation Oncology at the Massachusetts General Hospital (USA). A GPU implementation of DRR X-ray is also available. To mimic a parallel beam when generating the DRR with Plastimatch, SDD and SOD have been set to infinity. Resolving the centre parameter for the Plastimatch DRR program can be troublesome. As to not impede the validity of the experiment’s results, an objective function to optimise this parameter and an optimisation algorithm were utilised for a robust comparison.

2.5. Notebook 3: CT volume reconstructed from simulated data vs. original CT volume

The overall process is summarised in Figure 8. A CT scan acquisition is simulated. It consists of generating a series of X-ray projections around the virtual phantom at successive angles. We use the Core Imaging Library (CIL)⁷ to reconstruct the CT volumes from the projections [38]. It is a Python toolkit that provides many popular algorithms, including FBP and FDK. Slices of the reconstructed CT volume are then compared with the corresponding slices of the original CT volume.

2.6. Notebook 4: Registration of simulated radiographs onto real radiographs

Registration is the process of matching a moving dataset (called *source*) to a fixed dataset (called *target*). The source is somehow transformed (e.g. moved and/or deformed) so that it closely matches the target. Figure 9 illustrates the framework that is used to perform the registration. Our approach relies on fast X-ray image generation and robust global optimisation algorithms. The *source* (blue trace in Figure 9) is the surface model of the Lungman; and the target (red trace in Figure 9) is a real radiograph (see “ground truth” in Figure 14a). The virtual patient must match the location and orientation of the patient in

⁷<https://github.com/TomographicImaging/CIL>

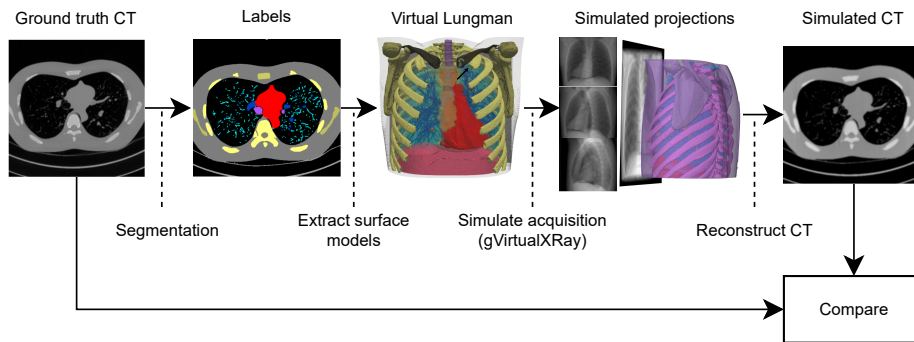


Figure 8: Flow chart demonstrating the validation of CT slices reconstructed from projections of the Lungman simulated with gVirtualXRay.

the real radiograph. The spatial resolution of the simulated radiograph must be the same as the real radiograph to allow a pixel by pixel comparison to quantify discrepancies and similarities. The position (and orientation) of the virtual patient, X-ray source and X-ray detector are unknown parameters (or inaccurate values stored in the Digital Imaging and Communications in Medicine (DICOM) header) that must be estimated by mathematical optimisation. Optimisation algorithms choose different combinations of parameters until a stopping criterion is met (green trace in Figure 9). At the end of the registration process, the corresponding simulated image should match the real radiograph.

Wen et al. [39, 14] showed the importance of choosing a robust global optimisation algorithm to perform the registration of the 3D surface model of a generic hand onto patient specific radiographs. The impact of the choice of objective function has also been demonstrated for the registration of surface models of tungsten fibres onto experimental X-ray projections [15].

Here we use one of today’s most popular global optimisation algorithm: covariance matrix adaptation evolution strategy (CMA-ES) [40]. It is a state-of-the-art global optimisation algorithm based on artificial evolution. It is designed for difficult non-linear non-convex optimisation problems in continuous domain. CMA-ES does not require a tedious parameter tuning for its application as finding suitable internal parameters is part of the algorithm design, which also makes it attractive. Only an initial solution and an initial standard deviation

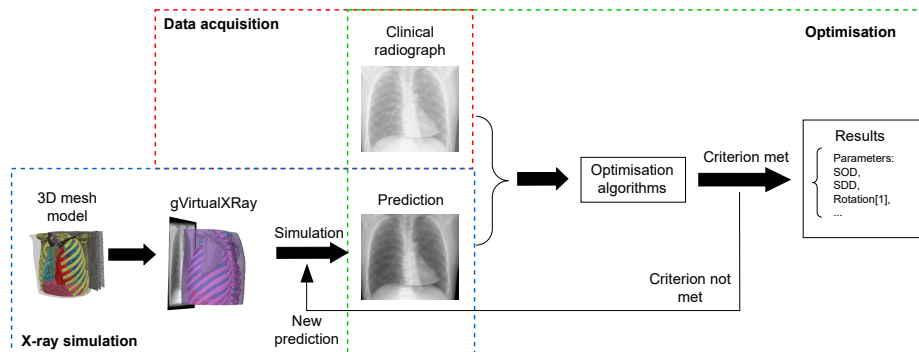


Figure 9: Illustration of the registration framework.

must be set by the user. The default population size is relatively small for fast convergence.

The objective function that we use is the root mean squared error (RMSE). Note that both the simulated and the ground truth images are corrected using the flat-field method. It is typically used to account for variations in beam homogeneity and in the pixel-to-pixel sensitivity of the detector. It is applied as follows:

$$\mathbf{Proj} = \frac{\mathbf{I} - \mathbf{D}}{\mathbf{F} - \mathbf{D}} \quad (5)$$

where \mathbf{I} is the raw X-ray image, \mathbf{Proj} corresponding image after flat-field correction, \mathbf{F} (full fields) and \mathbf{D} (dark fields) are projection images without sample and acquired with and without the X-ray beam turned on respectively. Flat-field correction allows comparison of images directly as they are now using comparable dynamic ranges. If \mathbf{I} , \mathbf{D} and \mathbf{F} are noiseless, then the pixel values of \mathbf{Proj} are between 0 and 1.

We use a digital radiograph (DR) of the Lungman anthropomorphic chest phantom. The image was taken with a clinical X-ray machine by GE Healthcare (Chicago, Illinois, USA) at one of our local hospitals (Glan Clwyd). Parameters relevant to the simulation are extracted from the DICOM file, such as kVp, filtration, SOD and SDD and refined by optimisation.

In clinical routine, post-processing is pre-defined. Using raw data from digital imaging is meaningless and does not simulate/replicate what occurs in current radiographic practice. Sharpening filters are applied to improve the readability of images. Standard clinical post processing algorithms were used for acquisition. No further post processing was undertaken following the acquisition such as image manipulation in terms of contrast and sharpness. Each manufacturer has its own proprietary post-processing algorithm, which is undisclosed. In our simulation, we calibrate a flexible sharpening filter (see Eq. 6) to mimic what is common practice in clinical routine. This calibration is performed by optimisation using CMA-ES. However, it is expected that the final simulated result will slightly differ from the ground truth as two different image

post-processing filters were used. We also expect that the image with post-processing will be more similar to the ground truth than the image without post-processing.

$$f_s(x, y) = f(x, y) + \alpha(f(x, y) - \bar{f}(x, y)) \quad (6)$$

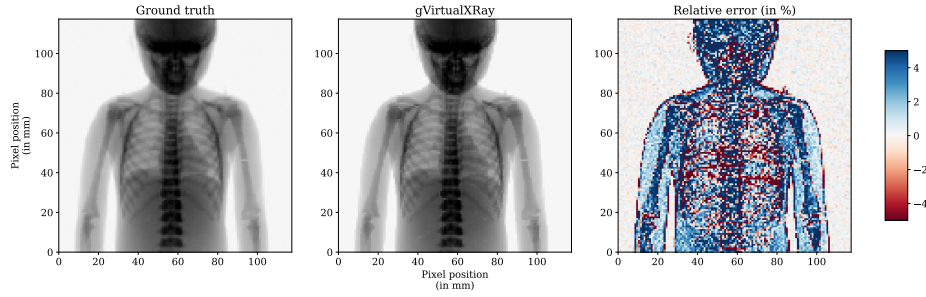
with f_s the sharpened image of f , and \bar{f} a smoothed version of f . We use a Gaussian filter to generate \bar{f} . α is a multiplicative factor that controls the amount of details ($f - \bar{f}$) that must be added back to f . The variance of the Gaussian filter and α are tuned by optimisation.

3. Results

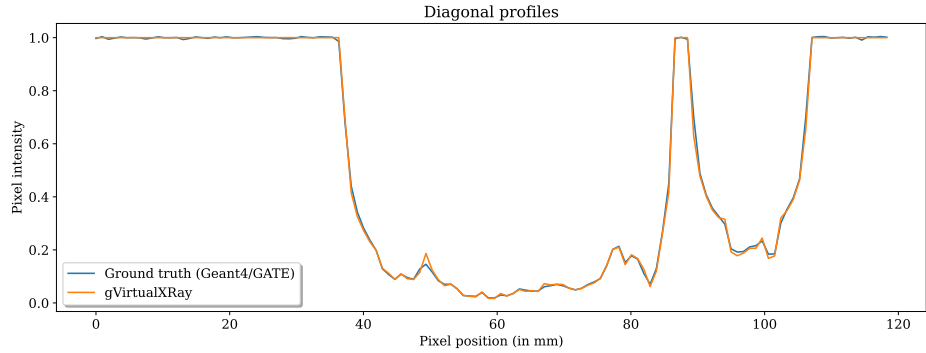
Table 2 provides a summary of the quantitative results. For all the tests that were conducted, the mean absolute percentage error (MAPE) is 3.20 ± 1.58 , the zero-mean normalised cross-correlation (ZNCC) is 99.08 ± 0.56 and the structural similarity index (SSIM) is 0.88 ± 0.13 . MAPE is relatively close to 0%, ZNCC to 100% and SSIM to 1: radiographs simulated with gVirtualXray closely match those computed with GATE or Plastimatch, and an actual digital radiograph; and the CT slices reconstructed from images simulated with gVirtualXray closely match those of an experimental scan. The corresponding standard deviation values are low: the results are consistent.

Table 2: Summary of the comparison between the images generated with gVirtualXray and their corresponding ground truth for all the test cases.

Notebook	Test	Ground truth	MAPE (in %)	ZNCC (in %)	SSIM	Resolution (in pixels)	Triangles	Runtime Ground truth (in ms)	Runtime gVirtualXray (in ms)	Speedup
1	Paediatric phantom	Monte Carlo	3.12	99.96	0.99	128 × 128	3,552,778	8.68E+08	23 ± 3	37,739,130
2	Lungman AP view	DRR	2.43	99.31	0.93	725 × 426	23,722,716	402 ± 6	42 ± 2	10
2	Lungman RL view	DRR	1.76	99.66	0.98	725 × 426	23,722,716	407 ± 6	42 ± 2	10
3	Lungman (1st slice)	CT	5.50	98.96	0.62	512 × 512	23,722,716	N/A	59	N/A
3	Lungman (middle slice)	CT	5.01	98.44	0.78	512 × 512	23,722,716	N/A	59	N/A
3	Lungman (last slice)	CT	4.46	99.05	0.82	512 × 512	23,722,716	N/A	59	N/A
4	Lungman PA view without post-processing	DR	1.78	98.34	0.94	1871 × 1881	N/A	20,973,540	314 ± 15	N/A
4	Lungman PA view with post-processing	DR	1.56	98.91	0.94	1871 × 1881	N/A	20,973,540	452 ± 66	N/A
Overall			3.20 ± 1.58	99.08 ± 0.56	0.88 ± 0.13					



(a) MAPE: 3.12%, ZNCC: 99.96%, and SSIM: 0.99.



(b) Corresponding diagonal intensity profiles.

Figure 10: Comparison between X-ray projections simulated with GATE and gVirtualXRay. For a fair comparison, each image is displayed using the same look-up table.

3.1. Beam spectrum, detector energy response and anatomically realistic digital phantom: GATE vs gVirtualXRay

In this test, the paediatric phantom from the ERROR project is used. For the Monte-Carlo simulations, the number of photons impinging the detector was set to 10^9 . The intensity profile of the MC simulation in Figure 10b shows that the number of photons is appropriate to generate a relatively noise-free image. About 10 days of computations were required on the test computer. For gVirtualXRay, 3,552,778 triangles were used. The simulated image is 128×128 pixels. However, one can note that the digital phantom used in GATE is made of voxels, and of triangles in gVirtualXRay.

Image comparison metrics indicate that the images are similar: ZNCC is

99.96%; MAPE is 3.12%, and SSIM is 0.99. Figure 10a shows that the simulations are visually close. The corresponding diagonal intensity profiles in Figure 10b are overlapping.

3.2. Simulated radiographs vs DRRs of a real CT scan of the Lungman Phantom

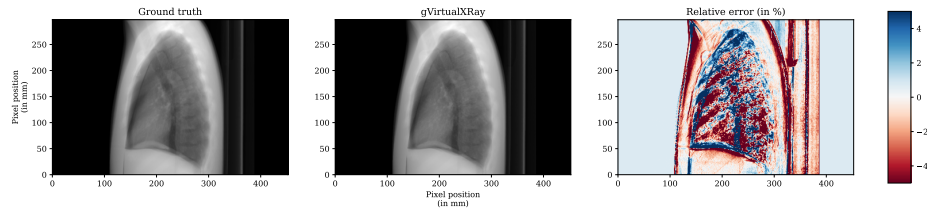
To compare the simulated X-ray radiographs, two DRR images are generated from the original CT volume. Clinically relevant views are considered: a right lateral (RL) chest view (Figure 11a) and an erect anteroposterior (AP) chest view (Figure 11c).

Images generated with gVirtualXray are very similar to those computed with Plastimatch, despite the use of homogeneous materials in the simulation. MAPE is low in both cases; ZNCC and SSIM are high in both cases. Intensity profiles in Figures 11b and 11d are overlapping except at the boundary of some structures. It indicates a possible misplacement of boundaries during the segmentation of the CT volume and the surface extraction from the segmentations. It took 432 ms to compute the DRR images on GPU with Plastimatch, 42 ms with gVirtualXray. It corresponds to a $10\times$ speedup.

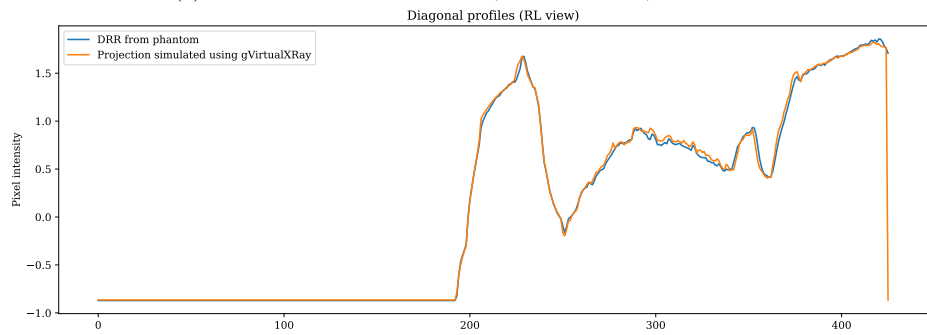
3.3. CT volume reconstructed from simulated data

Figure 12 displays the image comparison for the first, middle and last slices of the two volumes. The slices reconstructed from the simulated data are close to the original data. Hounsfield values are comparable. ZNCC is above 98.40% in all cases. It indicates a good level of correlation between the two volumes.

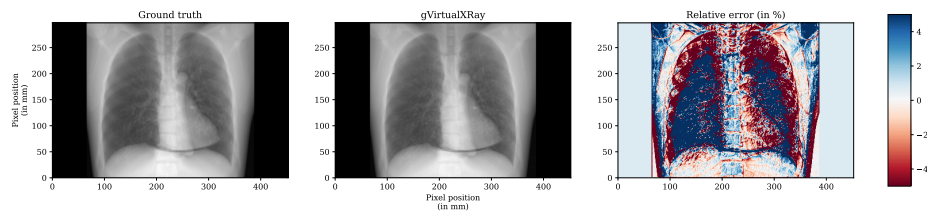
MAPE is between 4.50 and 5.5%, which may be acceptable. SSIM is between 0.62 and 0.82, which might be considered a bit low. A visual inspection of Figures 12a and 12b show the error is concentrated on the boundary between structures of significantly different HU values. This might be due to the difficulty to locate the border between structures with an accuracy of 1 pixel or the use of mathematical morphology to clean the segmentations. Figure 12c shows that highly inhomogeneous structures such as bone are hard to segment and approximate into a small set of homogeneous objects.



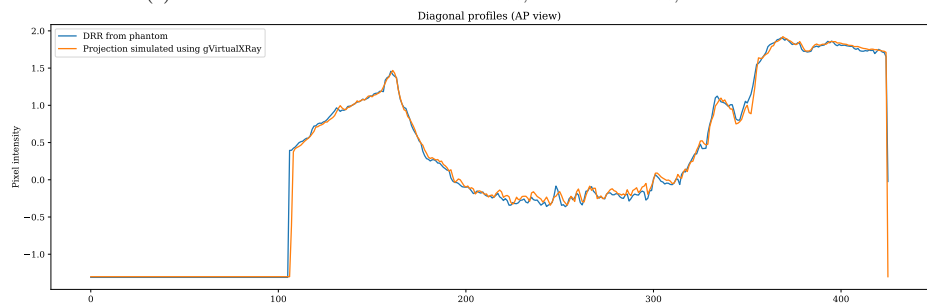
(a) RL chest view: MAPE: 1.76%, ZNCC: 99.66%, SSIM: 0.98.



(b) Diagonal intensity profiles corresponding to the images in Figure 11a.

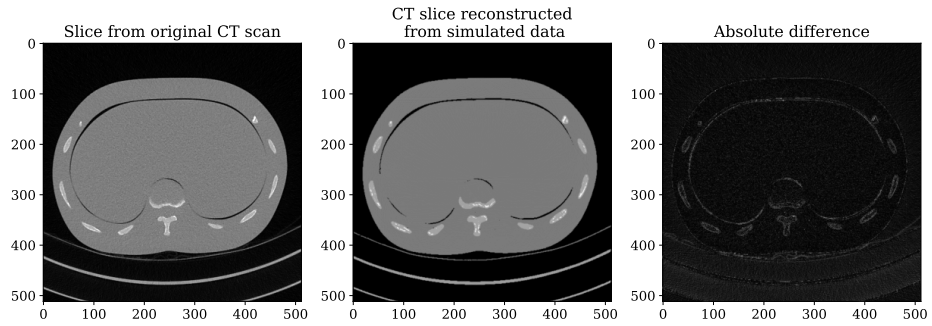


(c) Erect AP chest view: MAPE: 2.43%, ZNCC: 99.31%, SSIM: 0.93.

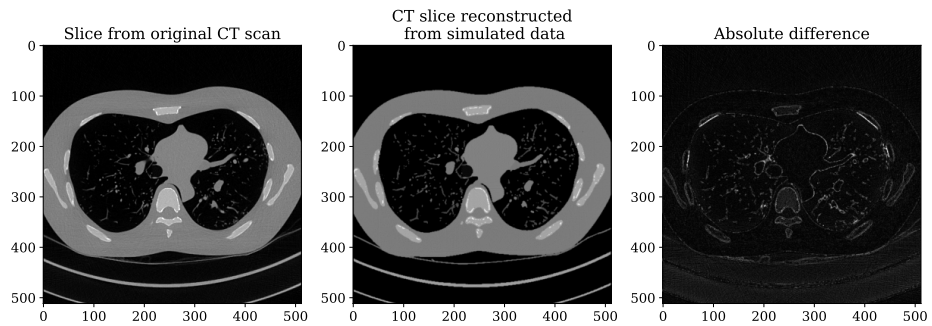


(d) Diagonal intensity profiles corresponding to the images in Figure 11c.

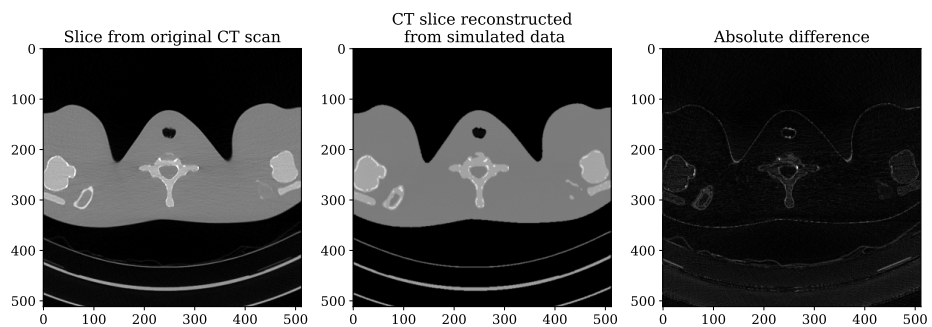
Figure 11: Comparison between X-ray projections simulated with gVirtualXray and DRR images generated with Plastimatch. For a fair comparison, each image of a row is displayed using the same look-up table.



(a) First slice: MAPE: 5.50%, ZNCC: 98.96%, SSIM: 0.62.

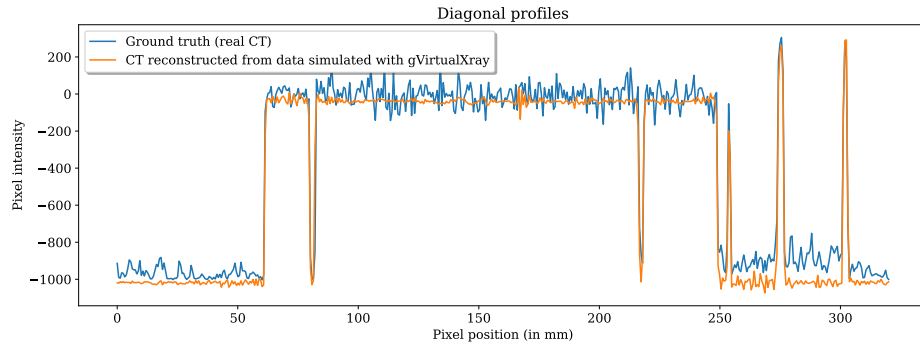


(b) First slice: MAPE: 5.01%, ZNCC: 98.44%, SSIM: 0.78.

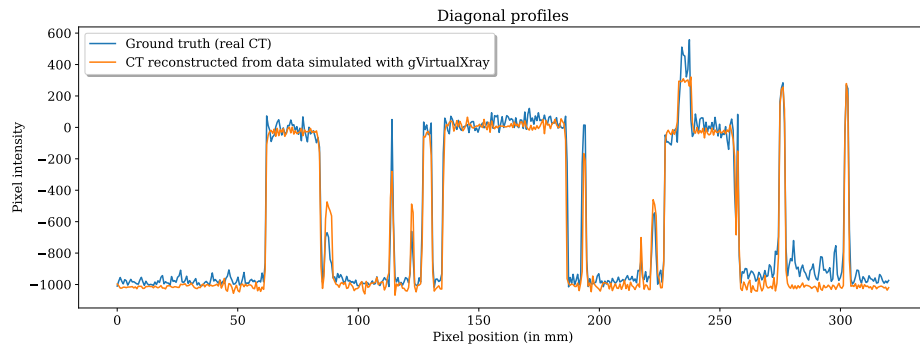


(c) First slice: MAPE: 4.46%, ZNCC: 99.05%, SSIM: 0.82.

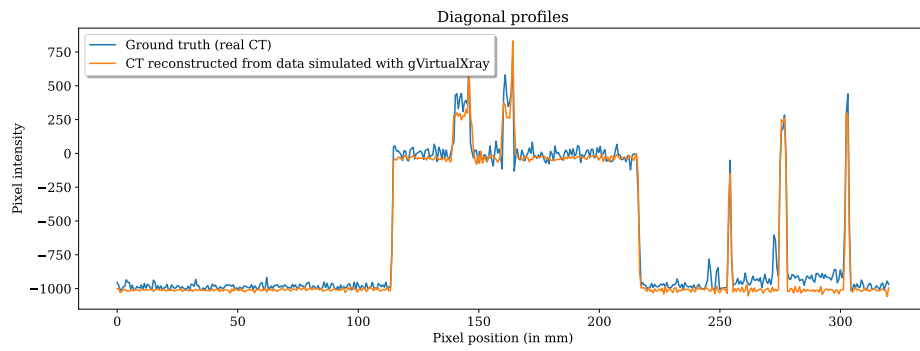
Figure 12: Comparison between CT slices reconstructed from simulated projections with slices from the original CT scan. For a fair comparison, all the images are displayed using the same look-up table.



(a)



(b)

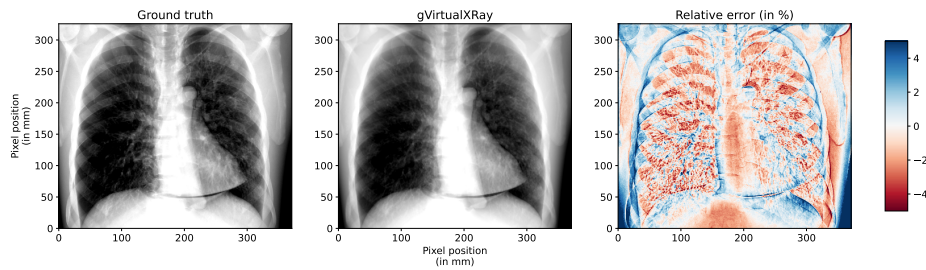


(c)

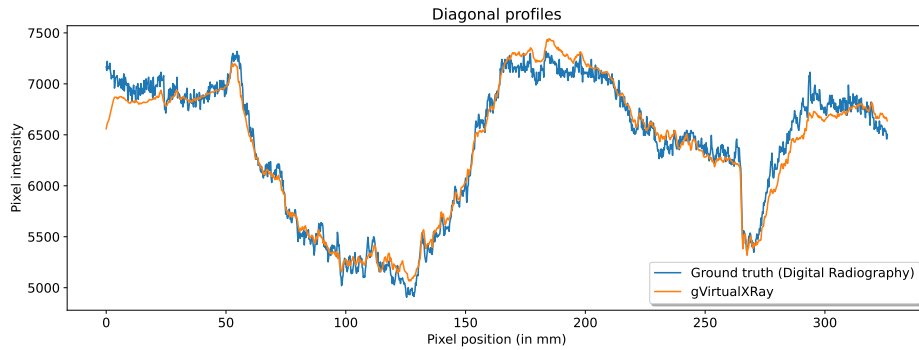
Figure 13: Diagonal profiles corresponding to the CT slices presented in Figure 12.

The corresponding diagonal profiles in Figure 13 indicate that the amplitude of Hounsfield Units is well recovered. The height of peaks and the depth of dips are accurate. We can see that the simulated data lacks photonic noise and that void was used instead of air. As we used $\mu_{air} = 0$, the HU values are equal to -1000 in the synthetic data whereas it should be slightly higher.

3.4. Registration of a Simulated Radiograph on a Real Digital Radiograph



(a) Posterior-anterior (PA) chest view: MAPE: 1.56%, ZNCC: 98.91%, and SSIM: 0.94.



(b) Corresponding diagonal intensity profiles.

Figure 14: Comparison between a registered X-ray projection simulated with gVirtualXray and a digital radiograph taken using a clinically utilised X-ray equipment. For a fair comparison, each image is displayed using the same look-up table.

In this test, a virtual Lungman phantom is registered so that its simulated radiograph closely matches a real digital radiograph taken with a clinical X-ray machine by GE Healthcare (Chicago, Illinois, USA). The position and orientation of the virtual Lungman phantom are first registered as an optimisation

problem to minimise the differences between the real radiograph and the simulated one.

Figure 14a shows the comparison between the simulated image and the real radiograph. We can see that the position and orientation of the Lungman have been successfully recovered. The pixel intensities are comparable. The use of post-processing slightly improves the results. ZNCC for the image was 98.34% without post-processing. It increases up to 98.91% with post-processing. The value is close to 100%. SSIM is 0.94 for both without and with post-processing, which is relatively close to 1. MAPE is 1.78% without post-processing, and 1.56% with post-processing, i.e. close to 0%.

From a numerical point of view, these results show that the simulated image is similar to the real X-ray radiograph acquired with a clinical equipment. The two images are visually comparable. The intensity profiles in Figure 14b are overlapping. They also show that the errors tend to be at the boundary between some anatomical structures, in particular the ribs, which is an issue that was highlighted in the previous sub-section. This is likely due to the series of discretisations that was needed to convert a tangible phantom into a suitable digital model: i) CT scan of the phantom, ii) segmentation of the CT scan, iii) cleaning of the segmentations, iv) surface extractions from the segmentation, and v) the use of homogeneous material properties. Each step may have introduced small numerical inaccuracies or a small misplacement of the boundaries. Nevertheless, pixel intensities are comparable in both images.

4. Discussion

Simulations, deterministic or MC, are approximations of real physics phenomena. Users of such simulations must always consider the context in which they want to deploy the simulation and understand the trade-offs that must be made. The need for accuracy will be greater for treatment planning in radiotherapy and in this case, MC will be preferred. Speed would be favoured in real-time VR for training purposes [11, 12, 13] and high-throughput data

applications [14, 20, 15, 16, 17]. The accuracy (or inaccuracy) of simulations depends on the mathematical model used and the simplifications made. For example, disabling scattering may not be suitable for thicker patients whereas it may be acceptable for thinner patients. The geometrical and material composition of the different structures that are imaged must be considered with care, in particular for inhomogeneous structures. For example, bones are complex to segment as they are made of hard and soft components that cannot be easily distinguished. Oversegmentation may improve the simulation fidelity but it will decrease the computational performance. Other input parameters such as tube voltage and photonic noise may be important and can be calibrated on experimental images to improve fidelity.

It is not possible to fully replicate an X-ray radiograph taken with a modern clinical device used in radiology departments in simulations. Indeed, post-processing image filtering is applied automatically to improve image readability [41]. As such filters are proprietary and closed-source, we were not able to implement them. To address this issue, we implemented and calibrated a general purpose image sharpening filter. The final simulated image is more realistic than without, but it is not a virtual copy of the actual image. Note that onboard imaging (OBI) or electronic portal imaging devices (EPIDs) available on linear accelerators (LINACs) used in radiotherapy can provide radiographic images without post-processing. They are used to generate the CBCT volumes used in radiotherapy.

Although the use of anthropomorphic phantoms provides a baseline for comparison in medical imaging, they are not real patient images and therefore this needs to be further validated using a range of patient CT images to capture varying attenuation from various body parts. A phantom represents an average body habitus only. The phantom does however provide uniform materials tissue-equivalent materials using synthetic bone used and lung tissues simulated using urethane foam. This allows multiple exposures with different acquisition parameters using the same phantom allowing changes in image quality and radiation dose to be identified as opposed to being influenced by patient factors

such as body composition.

Owing to the harmful effects of radiation, training and education of radiographic students require strict supervision under numerous radiation governance policies including working under the Ionising Radiation (Medical Exposure) Regulations (IRMER) 2017. This restricts students as they do not have the autonomy to work independently and learn from mistakes such as exposure parameter errors. It is therefore important that simulation is available for students to experiment upon without the ethical constraints within clinical practice. This allows them to develop into independent practitioners. With the Covid19 pandemic – the call for more simulation models for students and staff is necessary as clinical time may be limited with reduced patient contact. One of the ways to enhance clinical competence is through Medical Simulation training. This type of training has been proven to have many advantages which help improve medical practitioners’ competencies, and in return, improve patient safety and reduce health care costs. This is even more paramount in radiology owing to the harmful effects of radiation. X-ray and CT techniques cannot be experimented upon on real patients and therefore the effect of modifying acquisition parameters on image quality and radiation dose can only be visualised and demonstrated using simulation.

However, in the teaching and learning context, images must be simulated almost instantly when acquisition parameters are changed. There is well-established a consensus in the human-computer interaction (HCI) community that 1 second is the upper limit for the users to feel that the computer is causing the results of their actions [42, 43]. Any delay longer than one second will be considered unacceptable by the user. It is important that images are accurate too. When scattering can be ignored, we demonstrated that gVirtualXray provides a suitable alternative to Monte Carlo simulations and DRRs computed from CT volumes. For thicker patients with more of scatter, such deterministic simulations may be too simplistic and may not be appropriate. To date, high-resolution and relatively noise-free images cannot be generated fast enough with Monte Carlo methods for real-time or high-throughput data applications.

Another advantage is the use of surface meshes instead of voxel data: character animation used in video games can be deployed to change the virtual patient’s pose, which is not feasible with DRRs computed directly from CT volumes.

The direct simulation of X-ray images from real CT volumes is not recommended with gVirtualXray. Indeed, each voxel would need to be converted into 12 triangles and the voxels sorted by HU value. A DRR software dedicated to voxelised data, such as Plastimatch, is likely to provide better computational performance. Today’s GPUs are designed to render millions of triangles to provide real-time video games with a high level of realism. This property of GPUs makes it possible to use volumetric meshes made of tetrahedrons. VR applications with soft tissue deformations and cutting may benefit from this method. Note that this approach is also of interest in material science to simulate an object under load.

5. Conclusion

Until now, core components of gVirtualXray were evaluated by comparing its simulated images with corresponding images simulated with GATE, but only using a simplistic test object [9]. This new paper benchmarked gVirtualXray with clinically realistic phantoms.

Accurate images that would take days using GATE can be generated in milliseconds with gVirtualXray for high-throughput data (e.g. real-time VR, image registration, and training/testing data generation for ML) when scattering can be ignored. Simulated projections can also be fed to a reconstruction algorithm to produce CT volumes. The use of surface models enables the combination of X-ray simulation with real-time soft-tissue deformation [44, 9] and character animation [45], which is hardly possible with DRRs computed directly from CT volumes.

This initial project allows for further developments by continually improving the simulation whilst in use, for example, mimicking exposure time and photon scattering from real images. The use of real patient images is the next phase to

further validate and smooth out the limitations of this existing software.

Funding

None.

Declaration of Competing Interest

The authors declare that they have no competing interests.

Statements of ethical approval

Not applicable.

Acknowledgement

We thank NVIDIA Corporation for the donation of the NVIDIA TITAN Xp GPU used in the development and validation of gVirtualXray, and Supercomputing Wales (<https://www.supercomputing.wales/>) for the use of its supercomputer. We also gratefully acknowledge the support from the IN2P3 Computing Centre (<https://cc.in2p3.fr/>).

Acronyms

AP anteroposterior.

CAD computer-aided design.

CBCT cone-beam computed tomography.

CERN European Organization for Nuclear Research.

CMA-ES covariance matrix adaptation evolution strategy.

CPU central processor unit.

CT computed tomography.

DICOM Digital Imaging and Communications in Medicine.

DR digital radiograph.

DRR digitally reconstructed radiograph.

EPID electronic portal imaging device.

ERROR pEdiatRic dosimetRy personalized platfORm.

FBP filtered-back projection.

FDK Feldkamp, Davis and Kress.

GLSL OpenGL Shading Language.

GPU graphics processor unit.

GUI graphical user interface.

gVXR gVirtualXray.

HCI human-computer interaction.

HU Hounsfield Unit.

ICRU International Commission on Radiation Units and Measurements.

ITK Insight Toolkit.

LINAC linear accelerator.

MAPE mean absolute percentage error.

MC Monte Carlo.

MSE mean squared error.

NDT nondestructive testing.

OBI onboard imaging.

PMMA polymethyl methacrylate.

RL right lateral.

RMSE root mean squared error.

SDD source-to-detector distance.

SOD source-to-object distance.

SSIM structural similarity index.

VR virtual reality.

VTK Visualization Toolkit.

ZNCC zero-mean normalised cross-correlation.

References

- [1] N. Freud, J.-M. Létang, D. Babot, A hybrid approach to simulate x-ray imaging techniques, combining Monte Carlo and deterministic algorithms, *IEEE Transactions on Nuclear Science* 52 (5) (2005) 1329–1334. doi:10.1109/TNS.2005.858223.
- [2] A. Badal, A. Badano, Accelerating Monte Carlo simulations of photon transport in a voxelized geometry using a massively parallel graphics processing unit, *Medical Physics* 36 (11) (2009) 4878–4880. doi:10.1118/1.3231824.
- [3] G. Mettivier, A. Sarno, Y. Lai, B. Golosio, V. Fanti, M. E. Italiano, X. Jia, P. Russo, Virtual clinical trials in 2D and 3D x-ray breast imaging and dosimetry: Comparison of CPU-based and GPU-based Monte Carlo codes, *Cancers* 14 (4) (2022). doi:10.3390/cancers14041027.
- [4] D. F. Bosman, V. G. Balcaza, C. Delgado, S. Principi, M. A. Duch, M. Ginjaume, Validation of the MC-GPU Monte Carlo code against the PENELOPE/penEasy code system and benchmarking against experimental conditions for typical radiation qualities and setups in interventional radiology and cardiology., *Physica Medica* 82 (2021) 64–71. doi:10.1016/j.ejmp.2021.01.075.
- [5] D. Sarrut, M. Bardiès, N. Bousson, N. Freud, S. Jan, J. M. Létang, G. Loudos, L. Maigne, S. Marcatili, T. Mauxion, P. Papadimitroulas, Y. Perrot, U. Pietrzyk, C. Robert, D. R. Schaart, D. Visvikis, I. Buvat, A review of the use and potential of the GATE Monte Carlo simulation code for radiation therapy and dosimetry applications, *Medical Physics* 41 (6) (2014) 064301. doi:10.1118/1.4871617.
- [6] D. Sarrut, M. Bała, M. Bardiès, J. Bert, M. Chauvin, K. Chatzipapas, M. Dupont, A. Etxebeste, L. M. Fanchon, S. Jan, G. Kayal, A. S. Kirov, P. Kowalski, W. Krzemien, J. Labour, M. Lenz, G. Loudos, B. Mehadji,

- L. Ménard, C. Morel, P. Papadimitroulas, M. Rafecas, J. Salvadori, D. Seiter, M. Stockhoff, E. Testa, C. Trigila, U. Pietrzyk, S. Vandenberghe, M.-A. Verdier, D. Visvikis, K. Ziemons, M. Zvolský, E. Roncali, Advanced Monte Carlo simulations of emission tomography imaging systems with GATE, *Physics in Medicine & Biology* 66 (10) (2021) 10TR03. doi:10.1088/1361-6560/abf276.
- [7] P. Duvauchelle, N. Freud, V. Kaftandjian, D. Babot, A computer code to simulate x-ray imaging techniques, *Nuclear Instruments and Methods in Physics Research Section B: Beam Interactions with Materials and Atoms* 170 (1) (2000) 245–258. doi:10.1016/S0168-583X(00)00185-3.
- [8] F. P. Vidal, M. Garnier, N. Freud, J. M. Létang, N. W. John, Simulation of x-ray attenuation on the GPU, in: *Proceedings of Theory and Practice of Computer Graphics 2009*, Eurographics Association, Cardiff, UK, 2009, pp. 25–32. doi:10.2312/LocalChapterEvents/TPCG/TPCG09/025-032.
- [9] F. P. Vidal, P.-F. Villard, Development and validation of real-time simulation of x-ray imaging with respiratory motion, *Computerized Medical Imaging and Graphics* 49 (2016) 1–15. doi:10.1016/j.compmedimag.2015.12.002.
- [10] G. R. Jaenisch, C. Bellon, U. Ewert, aRTist – analytical RT inspection simulation tool for industrial application, in: *17th World Conference on Nondestructive Testing*, 2008.
- [11] Z. Zuo, W. Y. Qian, X. Liao, P.-A. Heng, Position based catheterization and angiography simulation, in: *2018 IEEE 6th International Conference on Serious Games and Applications for Health (SeGAH)*, 2018, pp. 1–7. doi:10.1109/SeGAH.2018.8401369.
- [12] M. Racy, A. Barrow, J. Tomlinson, F. Bello, Development and validation of a virtual reality haptic femoral nailing simulator, *Journal of Surgical Education* 78 (3) (2021) 1013–1023. doi:10.1016/j.jsurg.2020.10.004.

- [13] A. Sújara, G. Kelly, M. García, F. Vidal, Projectional Radiography Simulator: an Interactive Teaching Tool, in: F. P. Vidal, G. K. L. Tam, J. C. Roberts (Eds.), *Computer Graphics and Visual Computing (CGVC)*, The Eurographics Association, 2019, pp. 125–128. doi:10.2312/cgvc.20191267.
- [14] T. Wen, R. P. Mihail, F. P. Vidal, 3D-2D registration using x-ray simulation and CMA-ES, in: P. A. Castillo, J. L. Jiménez Laredo (Eds.), *Applications of Evolutionary Computation*, Springer International Publishing, Cham, 2021, pp. 453–468.
- [15] F. P. Vidal, I. T. Mitchell, J. M. Létang, Use of fast realistic simulations on GPU to extract CAD models from microtomographic data in the presence of strong CT artefacts, *Precision Engineering* 74 (2022) 110–125. doi:10.1016/j.precisioneng.2021.10.014.
- [16] J. Lovitt, Estimating length statistics of aggregate fried potato product via electromagnetic radiation attenuation, Master’s thesis, Boise State University, Idaho, USA (2016).
URL <https://scholarworks.boisestate.edu/td/1211>
- [17] M. Haiderbhai, S. Ledesma, S. C. Lee, M. Seibold, P. Fürnstahl, N. Navab, P. Fallavollita, pix2xray: converting RGB images into x-rays using generative adversarial networks, *International Journal of Computer Assisted Radiology and Surgery* 15 (6) (2020) 973–980. doi:10.1007/s11548-020-02159-2.
- [18] F. Albiol, A. Corbi, A. Albiol, Densitometric radiographic imaging with contour sensors, *IEEE Access* 7 (2019) 18902–18914. doi:10.1109/ACCESS.2019.2895925.
- [19] F. P. Vidal, P.-F. Villard, Simulated motion artefact in computed tomography, in: K. Bühler, L. Linsen, N. W. John (Eds.), *Eurographics Workshop on Visual Computing for Biology and Medicine*, The Eurographics Association, 2015, pp. 213–214. doi:10.2312/vcbm.20151228.

- [20] E. Andreozzi, A. Fratini, D. Esposito, M. Cesarelli, P. Bifulco, Toward a priori noise characterization for real-time edge-aware denoising in fluoroscopic devices, *BioMedical Engineering OnLine* 20 (1) (2021) 36. doi:10.1186/s12938-021-00874-8.
- [21] A. Corbi, D. Burgos, F. Vidal, F. Albiol, A. Albiol, X-ray imaging virtual online laboratory for engineering undergraduates, *European Journal of Physics* 41 (1) (2019) 014001. doi:10.1088/1361-6404/ab5011.
- [22] J. Allison, K. Amako, J. Apostolakis, P. Arce, M. Asai, T. Aso, E. Bagli, A. Bagulya, S. Banerjee, G. Barrand, B. Beck, A. Bogdanov, D. Brandt, J. Brown, H. Burkhardt, P. Canal, D. Cano-Ott, S. Chauvie, K. Cho, G. Cirrone, G. Cooperman, M. Cortés-Giraldo, G. Cosmo, G. Cuttone, G. Depaola, L. Desorgher, X. Dong, A. Dotti, V. Elvira, G. Folger, Z. Francis, A. Galoyan, L. Garnier, M. Gayer, K. Genser, V. Grichine, S. Guatelli, P. Guèye, P. Gumplinger, A. Howard, I. Hřivnáčová, S. Hwang, S. Incerti, A. Ivanchenko, V. Ivanchenko, F. Jones, S. Jun, P. Kaitaniemi, N. Karakatsanis, M. Karamitros, M. Kelsey, A. Kimura, T. Koi, H. Kurashige, A. Lechner, S. Lee, F. Longo, M. Maire, D. Mancusi, A. Mantero, E. Mendoza, B. Morgan, K. Murakami, T. Nikitina, L. Pandola, P. Paprocki, J. Perl, I. Petrović, M. Pia, W. Pokorski, J. Quesada, M. Raine, M. Reis, A. Ribon, A. R. Fira, F. Romano, G. Russo, G. Santin, T. Sasaki, D. Sawkey, J. Shin, I. Strakovsky, A. Taborda, S. Tanaka, B. Tomé, T. Toshito, H. Tran, P. Truscott, L. Urban, V. Uzhinsky, J. Verbeke, M. Verderi, B. Wendt, H. Wenzel, D. Wright, D. Wright, T. Yamashita, J. Yarba, H. Yoshida, Recent developments in Geant4, *Nuclear Instruments and Methods in Physics Research Section A: Accelerators, Spectrometers, Detectors and Associated Equipment* 835 (2016) 186–225. doi:10.1016/j.nima.2016.06.125.
- [23] P. Arce, D. Bolst, D. Cutajar, S. Guatelli, A. Le, A. B. Rosenfeld, D. Sakata, M.-C. Bordage, J. M. C. Brown, P. Cirrone, G. Cuttone, L. Pandola, G. Petringa, M. A. Cortès-Giraldo, J. M. Quesada, L. Desorgher, P. Dondero, A. Mantero, A. Dotti, D. H. Wright, B. Faddegon,

- J. Ramos-Méndez, C. Fedon, S. Incerti, V. Ivanchenko, D. Konstantinov, G. Latyshev, I. Kyriakou, C. Mancini-Terracciano, M. Maire, M. Novak, C. Omachi, T. Toshito, A. Perales, Y. Perrot, F. Romano, L. G. Sarmiento, T. Sasaki, I. Sechopoulos, E. C. Simpson, Report on G4-Med, a Geant4 benchmarking system for medical physics applications developed by the Geant4 medical simulation benchmarking group, *Medical Physics* (May 2020). doi:10.1002/mp.14226.
- [24] G. W. Sherouse, K. Novins, E. L. Chaney, Computation of digitally reconstructed radiographs for use in radiotherapy treatment design, *International Journal of Radiation Oncology, Biology, Physics* 18 (3) (1990) 651–658. doi:10.1016/0360-3016(90)90074-T.
- [25] W. Birkfellner, R. Seemann, M. Figl, J. Hummel, C. Ede, P. Homolka, X. Yang, P. Niederer, H. Bergmann, Fast DRR generation for 2D/3D registration, in: J. S. Duncan, G. Gerig (Eds.), *Medical Image Computing and Computer-Assisted Intervention – MICCAI 2005*, Springer Berlin Heidelberg, Berlin, Heidelberg, 2005, pp. 960–967.
- [26] Y. Sakata, R. Hirai, K. Kobuna, A. Tanizawa, S. Mori, A machine learning-based real-time tumor tracking system for fluoroscopic gating of lung radiotherapy, *Physics in Medicine & Biology* 65 (8) (2020) 085014. doi:10.1088/1361-6560/ab79c5.
- [27] F. P. Vidal, M. Folkerts, N. Freud, S. Jiang, GPU accelerated DRR computation with scatter, *Medical Physics* 38 (6) (2011) 3455–3456. doi:10.1118/1.3611828.
- [28] T. Flohr, B. Ohnesorge, *Multi-slice and Dual-source CT in Cardiac Imaging: Principles — Protocols — Indications — Outlook*, Springer, Berlin, Heidelberg, 2007, Ch. Multi-slice CT Technology, pp. 41–69. doi:10.1007/978-3-540-49546-8_3.
- [29] F. P. Vidal, M. Garnier, N. Freud, J. M. Létang, N. W. John, Accelerated deterministic simulation of x-ray attenuation using graphics hardware, in:

- Eurographics 2010 - Poster, Eurographics Association, Norrköping, Sweden, 2010, p. Poster 5011.
- [30] N. Freud, P. Duvauchelle, J. M. Létang, D. Babot, Fast and robust ray casting algorithms for virtual x-ray imaging, *Nuclear Instruments and Methods in Physics Research Section B: Beam Interactions with Materials and Atoms* 248 (1) (2006) 175–180. doi:10.1016/j.nimb.2006.03.009.
- [31] P. Papadimitroulas, W. D. Erwin, V. Iliadou, T. Kostou, G. Loudos, G. C. Kagadis, A personalized, monte carlo-based method for internal dosimetric evaluation of radiopharmaceuticals in children, *Medical Physics* 45 (8) (2018) 3939–3949. doi:10.1002/mp.13055.
- [32] W. Schroeder, K. Martin, B. Lorensen, *The Visualization Toolkit – An Object-Oriented Approach To 3D Graphics*, 4th Edition, Kitware, Inc., 2006.
- [33] D. R. White, J. Booz, R. V. Griffith, J. J. Spokas, I. J. Wilson, Report 44, *Journal of the International Commission on Radiation Units and Measurements* os-23 (1) (Jan. 2019). doi:10.1093/jicru/os23.1.Report44.
- [34] S. Rodriguez Perez, N. Marshall, L. Struelens, H. Bosmans, Characterization and validation of the thorax phantom lungman for dose assessment in chest radiography optimization studies, *Journal of Medical Imaging* 5 (2018) 1. doi:10.1117/1.JMI.5.1.013504.
- [35] M. McCormick, X. Liu, L. Ibanez, J. Jomier, C. Marion, ITK: enabling reproducible research and open science, *Frontiers in Neuroinformatics* 8 (2014) 13. doi:10.3389/fninf.2014.00013.
- [36] W. Schneider, T. Bortfeld, W. Schlegel, Correlation between CT numbers and tissue parameters needed for Monte Carlo simulations of clinical dose distributions, *Physics in Medicine & Biology* 45 (2) (2000) 459–478. doi:10.1088/0031-9155/45/2/314.

- [37] G. Sharp, R. LI, J. Wolfgang, G. Chen, M. Peroni, M. Spadea, S. Mori, J. Zhang, J. Shackelford, N. Kandasamy, Plastimatch – an open source software suite for radiotherapy image processing, in: Proceedings of the XVI'th International Conference on the use of Computers in Radiotherapy (ICCR), Amsterdam, Netherlands, 2010.
- [38] J. S. Jørgensen, E. Ametova, G. Burca, G. Fardell, E. Papoutsellis, E. Pasca, K. Thielemans, M. Turner, R. Warr, W. R. B. Lionheart, P. J. Withers, Core Imaging Library - Part I: a versatile Python framework for tomographic imaging, *Philosophical Transactions of the Royal Society A: Mathematical, Physical and Engineering Sciences* 379 (2204) (2021) 20200192. [arXiv:https://royalsocietypublishing.org/doi/pdf/10.1098/rsta.2020.0192](https://royalsocietypublishing.org/doi/pdf/10.1098/rsta.2020.0192), doi:10.1098/rsta.2020.0192.
- [39] T. Wen, R. Mihail, s. Al-maliki, J. Letang, F. Vidal, Registration of 3D triangular models to 2D x-ray projections using black-box optimisation and x-ray simulation, in: F. P. Vidal, G. K. L. Tam, J. C. Roberts (Eds.), *Computer Graphics and Visual Computing (CGVC)*, The Eurographics Association, 2019, pp. 105–113. doi:10.2312/cgvc.20191265.
- [40] N. Hansen, Benchmarking a BI-population CMA-ES on the BBOB-2009 function testbed, in: *Workshop Proceedings of the GECCO Genetic and Evolutionary Computation Conference*, ACM, 2009, pp. 2389–2395.
- [41] E. Seeram, D. Seeram, Image postprocessing in digital radiology – A primer for technologists, *Journal of Medical Imaging and Radiation Sciences* 39 (1) (2008) 23–41. doi:10.1016/j.jmir.2008.01.004.
- [42] R. B. Miller, Response time in man-computer conversational transactions, in: *Proceedings of the December 9-11, 1968, Fall Joint Computer Conference, Part I, AFIPS '68 (Fall, part I)*, Association for Computing Machinery, New York, NY, USA, 1968, p. 267–277. doi:10.1145/1476589.1476628.

- [43] S. K. Card, G. G. Robertson, J. D. Mackinlay, The information visualizer, an information workspace, in: Proceedings of the SIGCHI Conference on Human Factors in Computing Systems, CHI '91, Association for Computing Machinery, New York, NY, USA, 1991, p. 181–186. doi:10.1145/108844.108874.
- [44] P.-F. Villard, F. P. Vidal, C. Hunt, F. Bello, N. W. John, S. Johnson, D. A. Gould, A prototype percutaneous transhepatic cholangiography training simulator with real-time breathing motion, *International Journal of Computer Assisted Radiology and Surgery* 4 (6) (2009) 571–578. doi:10.1007/s11548-009-0367-1.
- [45] A. Sujar, G. Kelly, M. García, F. P. Vidal, Interactive teaching environment for diagnostic radiography with real-time x-ray simulation and patient positioning, *International Journal of Computer Assisted Radiology and Surgery* 17 (1) (2022) 85–95. doi:10.1007/s11548-021-02499-7.